

Spin-dependent multilevel interactions at a nonmagnetic/magnetic MoSe₂/VSe₂ van der Waals interface and multifunctional properties

Meng-Xue Ren, Yue-Jiao Zhang, Yu-Meng Gao, Mei-Yan Tian, Chen-Dong Jin, Hu Zhang, Ru-Qian Lian, Peng-Lai Gong, Rui-Ning Wang , Jiang-Long Wang, * and Xing-Qiang Shi [†]

Key Laboratory of Optic-Electronic Information and Materials of Hebei Province, Hebei Research Center of the Basic Discipline for Computational Physics, College of Physics Science and Technology, Hebei University, Baoding 071002, People's Republic of China



(Received 14 August 2023; revised 19 December 2023; accepted 21 December 2023; published 16 January 2024)

Since the theoretical and experimental demonstration of the quasibonding (QB) interactions between van der Waals (vdW) layers of two-dimensional (2D) materials, diverse effects and applications of interlayer and interface QB in vdW homo- and heterostructures have been reported. However, for vdW heterostructures (vdWHs) composed of magnetic and nonmagnetic 2D layers, the principles of interlayer QB interaction in these systems and their potential application remain to be elucidated. In the current work, by density functional theory calculations combined with crystal orbital Hamiltonian population analysis, the spin-dependent and multilevel interlayer QB (namely, orbital hybridization) in a *H*-MoSe₂/*H*-VSe₂ nonmagnetic/magnetic vdWH is established, and its multifunctional properties for spintronics and spin-dependent optoelectronics are revealed. In particular, (1) the two spin channels have distinct interlayer interactions: spin-up is a two-level interaction while three energy levels are involved in spin-down; for each level, multiorbitals (mainly *s*, *p_z*, and *d_{z²}* orbitals) make contributions to the interlayer interaction; (2) distinct band alignment types ranging from type I and type II to a mixed type appear; and (3) the interlayer interaction makes the VSe₂ layer have better bipolar magnetic semiconductor properties. Our current work demonstrates the orbital-resolved multilevel analysis as a powerful tool for understanding the interlayer QB interaction and indicates the potential of the MoSe₂/VSe₂ vdWH for multifunctional applications.

DOI: [10.1103/PhysRevB.109.045420](https://doi.org/10.1103/PhysRevB.109.045420)

I. INTRODUCTION

The van der Waals homo- and heterostructures (vdWHs) based on two-dimensional (2D) layered materials, especially metal/2D semiconductor junctions (MSJs) and 2D semiconductor heterojunctions (SHJs), have diverse potential applications in the fields of electronics and optoelectronics [1–4], spintronics [5,6], valleytronics [7,8], twistronics [9], and photocatalysis [10,11], etc. For the interlayer interactions in vdWHs, in addition to the London dispersion attraction of vdW force [12], the interlayer orbital hybridization leads to the common existence of covalentlike quasibonding (QB) interaction between 2D layers [13–15]. The QB interaction is similar to the Pauli-repulsion part of the vdW interaction (considering a Lennard-Jones-like potential), and the QB between 2D layers also gives a significant energy-level splitting on the order of 1 eV [13]; for a recent review, see Ref. [16]. Interlayer QB exhibits two main characteristics that are like covalent bonds but weaker than typical chemical bonds, namely, the redistribution of electron density and the formation of bonding and antibonding states between vdW layers [13,15,17]. The QB between 2D and mixed-dimensional vdWHs [18,19] not only changes the intrinsic properties of subsystems, but it also greatly affects the diverse applications of the vdWHs, such as

modifying the electronic structure including direct to indirect gap transition, and engineering the electrical [20], optical [21], and ferroelectric [22] properties.

Since the theoretical [13] and experimental [17] demonstration of the QB interactions between 2D materials, many studies have reported that interlayer QB interactions can affect the vibration modes [23], magnetism [24–28], and optical absorption and photoluminescence [13,29–31] of 2D materials. In MSJs, QB could have a significant impact on the Schottky barrier height [19,32]. In SHJs, the interlayer QB interactions influence the band alignments [33]; a practical screening method including QB effects is proposed to construct robust momentum-matched heterojunctions [34]. For vdWHs composed of magnetic and nonmagnetic 2D layers, studies report that they have robust ferromagnetism [35] and potential applications as spin valves [36] and magnetic tunnel junctions [37], properties tuning by strain and electric field [38,39], and the magnetic proximity effect and valleytronics properties [7,8,40]. Although nonmagnetic/magnetic vdWHs have been studied a lot, the principles of the interlayer QB interaction in these systems and the properties tuning by QB and more potential application remain to be elucidated. Note that the studies of the asymmetric magnetic proximity effect and valley splitting [7,8] focused on the *K* point of the Brillouin zone; here we focus on the Γ point where the interlayer QB (orbital hybridization) is much stronger than that at the *K* point.

In the current work, using density functional theory (DFT) calculations combined with crystal orbital Hamiltonian

*jllwang@hbu.edu.cn

[†]shixq20hbu@hbu.edu.cn

population (COHP) analysis [41], we study in detail the spin-dependent interlayer interactions in the MoSe₂/VSe₂ nonmagnetic/magnetic vdWH with emphasis on the multi-level interaction, and each energy level has more than one atomic orbital involved in the interaction. We find that the interlayer interaction affects both sides of the vdWH: (1) significant spin splitting is introduced to the originally nonmagnetic MoSe₂ side and, for the valence band at the Γ point, the two spin channels of MoSe₂ have distinct orbital-interaction characteristics with VSe₂—spin-up is a two-level interaction while three levels are involved for spin-down; (2) the intrinsic magnetic properties of VSe₂ are largely maintained in vdWH after coupling with MoSe₂ and, for the VSe₂ side, the interlayer interaction makes the bipolar magnetic semiconductor (BMS) properties better with increased spin-flip gap and decreased transport gap. For the overall vdWH, the two spin channels have very different band alignment types ranging from type I and type II to type *H*—a mixed type at the critical point between types I and II [42]. The current study not only demonstrates the orbital-resolved multilevel analysis as a powerful tool for understanding orbital hybridization at the vdW interface, but also indicates the potential of the MoSe₂/VSe₂ vdWH for multifunctional applications.

II. METHODS

Spin-polarized DFT calculations were performed by using the Vienna *ab initio* simulation package (VASP) [43–45]. The projector augmented-wave potential was employed to describe the core electrons and the valence electron orbitals were expanded on a plane-wave basis with an energy cut-off of 500 eV [46]. The generalized gradient approximation in the Perdew-Burke-Ernzerhof form (GGAPBE) was used [47]. For the *3d* orbitals of vanadium atoms, Hubbard *U* was introduced, where *U* was 2 eV and *J* was 0.84 eV in the calculations [48,49]. The vdW interaction was considered by using the optB86b-vdW density functional of Dion *et al.* [50] and Klimeš *et al.* [51]. The convergence criteria for energy and force were set to 10⁻⁶ eV and 0.01 eV/Å, respectively. The *k*-point sampling of the 2D Brillouin zone adopted the Monkhorst-Pack scheme [52] with a grid mesh of 15 × 15. The vacuum separation in the vertical direction was 15 Å to ensure that the interaction between periodic images was negligible. For bonding analysis of interlayer interactions, the LOBSTER package [53–56] was used, which gives crystal orbital Hamiltonian population (COHP) [57] via weighting the density of states (DOS) by the corresponding Hamiltonian matrix elements. The multilevel and multiorbital analysis can be achieved from the orbital-pair COHP analysis projected to orbital-pair interactions for the valence and conductance bands of interest at the Γ point [58] in combination with the real-space wave-function plot of these bands at the Γ point. More on the calculation of COHP can be found in the Supplemental Material [59]; also see Refs. [60–73]. We checked the band structure by considering spin-orbit coupling (SOC) to make sure that the main conclusion holds. The VASPKIT program was used for postprocessing of the electronic structure data [74]. More calculation details can be found in the related sections.

III. RESULTS AND DISCUSSION

To investigate the interlayer QB of a nonmagnetic/magnetic vdWH, the *H*-phase nonmagnetic MoSe₂ and magnetic VSe₂ are adopted as the typical example. The *H*-phase VSe₂ can be selectively grown and is more thermodynamically favorable than the *T* phase at the 2D limit [75]. The relaxed lattice constants of MoSe₂ and VSe₂ are 3.32 and 3.33 Å, respectively, indicating negligible lattice mismatch between these two monolayers. To select a suitable stacking configuration, we consider six high-symmetry stacking configurations (for details see “More on stacking configuration” in the Supplemental Material [59]). We calculate the binding energy (E_{bind}) and phonon spectrum of the *H*-MoSe₂/*H*-VSe₂ heterostructure to discuss the dynamical and thermal stability as was done in [28]. For the binding energy, we use the equation $E_{\text{bind}} = E_{\text{total}} - E_{\text{VSe}_2} - E_{\text{MoSe}_2}$. The E_{bind} is calculated to be -0.235 eV/cell, suggesting the energetic and thermal stability of forming the heterostructure. The binding energy per unit area is -24.9 meV/Å², which is comparable to that of typical 2D materials [76]. Figure S3 [59] indicates that the structure of *H*-MoSe₂/*H*-VSe₂ does not have imaginary frequencies, indicating the dynamical stability of the heterostructure. To determine the interface spacing of the MoSe₂/VSe₂ vdWH ($d_{\text{Se-Se}}$ for the Se atoms across the vdW gap), the binding energy curve as a function of $d_{\text{Se-Se}}$ is calculated (Fig. S4 [59]) and the equilibrium spacing is 3.15 Å. The relaxed structure is shown in Fig. 1(g).

A. Spin-dependent interlayer QB interaction

The isolated monolayers of group-VI transition metal dichalcogenide (TMD), *H*-MoSe₂, and group-V TMD, *H*-VSe₂, have very different electronic structures due to the vanadium atom lacking one electron as well as the on-site Coulomb repulsion of vanadium *3d* electrons. The valence band (VB) of MoSe₂ is spin paired (Figs. 1(a) and S5a [59]) while that in VSe₂ becomes the fully spin-polarized VB and conduction band (CB) with a spin splitting of ~1.26 eV (Figs. 1(c) and S5(b) [59]), and similar to that reported in the literature [48]. Figure 1(h) shows the Brillouin zone with high-symmetry *k* points for band structure plots.

Figures 1(a) and 1(c) show the subsystem band structures projected to the Se-*p_z* orbital since the *p_z* orbital contributes to both Se-Se and Se-Mo(V) interlayer interactions, as indicated in Fig. 1(g) and Table I. A comparison of the band structure near the Fermi energy of the subsystems [Figs. 1(a) and 1(c)] with that of the vdWH [Fig. 1(b)] shows the interface orbital hybridization induced energy splitting of VB mainly at and around the Γ point. This kind of interlayer interaction is named covalentlike quasibonding (QB) in the literature [13] as discussed in the Introduction.

The interlayer QB in the MoSe₂/VSe₂ vdWH makes (1) the complicated band structure in Fig. 1(b) for the three VBs (the VB, VB-1, and VB-2 that are labeled) below the Fermi level, and (2) the CB energy shift at the Γ point relative to that of the isolated VSe₂. These above band-structure evolutions from subsystems to those in vdWH can be understood from the following aspects at and around the Γ point:

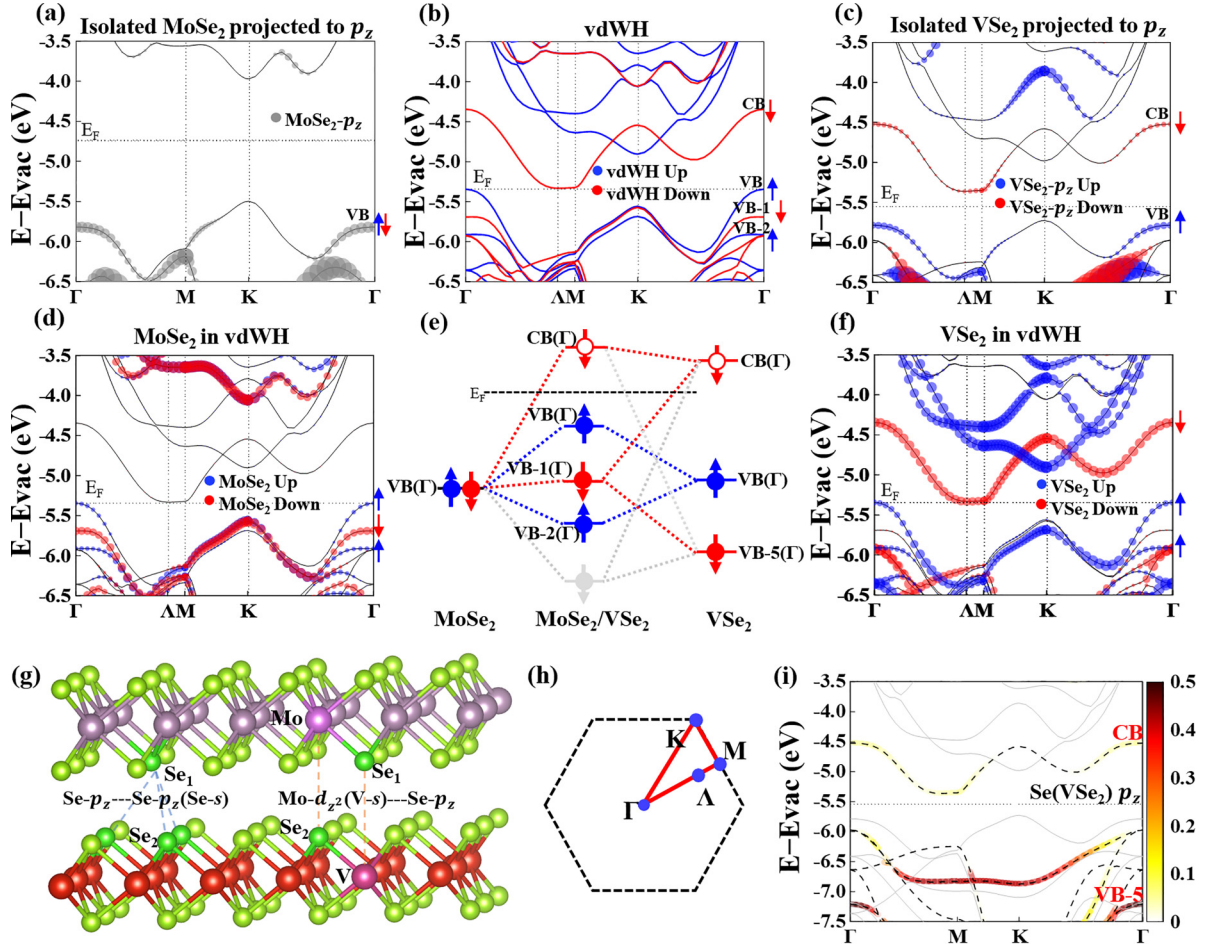


FIG. 1. Spin-dependent interlayer interaction in vdWH from projected band structures relative to vacuum level (E_{vac}). (a–c) Spin-polarized band structure of the vdWH and of the isolated subsystems MoSe₂ and VSe₂ with projection to the Se- p_z orbital. (d, f) the vdWH band structure projected to the MoSe₂ and VSe₂ layer, and (e) sketch for the spin-dependent energy-level hybridization of the MoSe₂ VB with the VSe₂ VB and CB at the Γ point, which is derived from the band structure plots. For spin-down, a deeper VSe₂ level [VB-5; refer to panel (i)] is also involved as indicated with gray. The dot sizes in projected band structures indicate the relative magnitude of projection. Blue (red) denotes spin-up (spin-down). In vdWH, the MoSe₂ and VSe₂ sides have slightly different E_{vac} 's and the averaged value is used. (g) Structure of the MoSe₂/VSe₂ vdWH with some of the interlayer orbital-pair interactions labeled. (h) Brillouin zone with the relevant k points indicated. (i) The VB-5 for spin-down of isolated VSe₂ with Se- p_z character at the Γ point; the scale indicates the magnitude of projection and the other spin (spin-up) is denoted with light gray lines.

(1) The interlayer orbital hybridization happens for bands with similar orbital character, namely, the VB of MoSe₂ and the spin-polarized VB and CB of VSe₂ at (and around) the Γ point that have the Se- p_z orbital character [Figs. 1(a)–1(c)] and S6 [59]. The d_{z^2} orbitals make less contribution to interlayer interaction than p_z does (Table I) due to the larger interlayer separation between Mo(V)–Se than Se–Se across the vdW gap, and hence the above discussion focuses on p_z .

(2) The layer-projected band structures in Figs. 1(d) and 1(f) show that VB, VB-1, and VB-2 at the Γ point [labeled in Fig. 1(b)] of vdWH are a mixture of bands from MoSe₂ and VSe₂; the spin-down CB is mainly from VSe₂. Among the three VBs of vdWH, the spin-down VB-1 is mainly from MoSe₂ while the spin-up VB and VB-2 are from both layers of VSe₂ and MoSe₂ [Figs. 1(d) and 1(f)]. Notably, spin polarization is induced into the MoSe₂ layer.

(3) The above discussions show that the spin-up channel has a more apparent interlayer interaction (layer mixing of

bands around the Γ point) than the spin-down channel (layer separation in bands). The spin-dependent band hybridization at the Γ point between the MoSe₂ VB and the VSe₂ VB and CB can be sketched as in Fig. 1(e). For spin-up, it is a two-level interaction, similar to that in the literature [14]. For spin-down, however, to explain the upshift of VB-1 in vdWH (relative to VB in MoSe₂), a third, deeper level [the VB-5(Γ) of VSe₂ as labeled in Fig. 1(i)] is also involved (will be elaborated upon later).

Table I summarizes the orbital-pair contributions to interlayer interaction. It is obtained from the orbital-projected COHP (p COHP) analysis, which partitions the band-structure energy into the contribution of orbital-pair interactions [54] and the magnitude of projected COHP hints at its relative contribution to the interlayer interaction (for details see “More on projected COHP” in the Supplemental Material [59]). We consider the orbital-pair interactions from the interlayer Se–Se and Se–Mo(V) pairs as illustrated in Fig. 1(g) for the

TABLE I. Orbital-pair contributions to the interlayer interaction at the Γ point from projected COHP. Only the orbital pairs that have relatively larger contributions are listed. Positive (negative) numbers mean antibonding (bonding). Numbers before (after) the comma indicate the interlayer interaction of spin-up VB (VB-2) or spin-down CB (VB-1). In vdWH, spin-up (spin-down) corresponds to VB, VB-2 (CB, VB-1) as shown in Fig. 1(e). Se_1 (Se_2) denotes the interface Se atoms from MoSe_2 (VSe_2); refer to Fig. 1(g).

Se–Se interaction ^a	$\text{Se}_1\text{-}p_z\text{-Se}_2\text{-}p_z$	$\text{Se}_1\text{-}p_z\text{-Se}_2\text{-}s$	$\text{Se}_1\text{-}s\text{-Se}_2\text{-}p_z$
Spin-up: VB, VB-2	0.21, –0.01	0.02, 0	0.02, 0
Spin-down: CB, VB-1	0.06, 0.11	0, 0.02	0.01, 0
Se– M interaction ^a	$\text{Se}_1\text{-}p_z\text{-}V\text{-}d_{z^2}$	$\text{Se}_1\text{-}p_z\text{-}V\text{-}s$	$\text{Se}_2\text{-}p_z\text{-}Mo\text{-}d_{z^2}$
Spin-up: VB, VB-2	0.02, –0.01	0, –0.01	0.02, 0
Spin-down: CB, VB-1	0.02, –0.01	0, –0.01	0, 0.01
Summation ^b	Sum of Se–Se	Sum of Se– M	Sum of ALL
Spin-up: VB, VB-2	0.75, –0.03	0.04, –0.02	0.79, –0.05
Spin-down: CB, VB-1	0.21, 0.39	0.02, –0.01	0.23, 0.38

^aThe orbital-pair interactions from the interlayer Se–Se and Se–Mo(V) interactions as illustrated in Fig. 1(g) for the Se, Mo, and V atoms close to the vdW interface. “ M ” means Mo or V atoms.

^bThe sum is over all orbital pairs and multiplied by the number of nearest-neighbor atoms between layers. Namely, the numbers for Se–Se interaction are multiplied by 3 in the summation.

Se, Mo, and V atoms close to the vdW interface. The interlayer Mo(V)–V(Mo) interaction is even smaller and hence neglected. In our DFT calculations, semicore electrons are considered for Mo(V), while for the below discussion of interlayer interactions (Table I), only valence orbitals are needed: namely, for Se, one $4s$ and three $4p$ orbitals and hence four orbitals are needed for the discussion of orbital-pair interactions; for Mo(V), one $5s$ ($4s$) and five $4d$ ($3d$) orbitals and hence six orbitals are needed for Mo(V). As a result, for Se–Se interactions, there are $4 \times 4 = 16$ matrix elements (or orbital-pair interactions), and for Se–Mo(V) interactions $4 \times 6 = 24$ matrix elements. In Table I, only the orbital pairs that have relatively larger contributions are listed.

Table I reveals that (1) the interlayer Se–Se interaction contributes most to the interlayer interaction and, in general, is much larger than interlayer Se– M interaction. (2) For the spin-up VB, and spin-down CB and VB-1 of vdWH, the $\text{Se}\text{-}p_z\text{-Se}\text{-}p_z$ interactions dominate the interlayer interaction, while for the spin-up VB-2, the Se–Se and Se–V interactions are comparable, and both the $V\text{-}s$ and $V\text{-}d_{z^2}$ orbitals are involved. These can be seen more intuitively from the real-space wave function plots in Figs. 2(d) and 3(d).

The interlayer QB interactions of the MoSe_2 VB with the spin-up and spin-down channels of VSe_2 lead to spin splitting also in MoSe_2 [Fig. 1(d)]. Next, we discuss the spin-dependent properties and the band alignments in vdWH for the two spin channels, which are useful for spin-dependent (opto)electronics [7] and photoelectric devices [77].

B. Spin-up and type H band alignment

For the spin-up channel, Figs. 2(a), 2(c), and 2(b) show the band structures of the two subsystems and that of vdWH projected to VSe_2 and MoSe_2 layers for spin-up, in which the VB of MoSe_2 hybridizes with the VB of VSe_2 and forms the VB and VB-2 in vdWH at the Γ point [refer to Fig. 1(e)]. The corresponding wave functions at the Γ point for the isolated subsystem VBs of MoSe_2 and VSe_2 , and for the vdWH VB and VB-2, can be found in Fig. 2(d).

The interlayer-antibonding state, VB in vdWH at the Γ point [refer to Figs. 2(b) and 2(d)], makes the original VB edge of MoSe_2 and VSe_2 shift up in energy and the valence band edge changes from the K point in the isolated monolayers to the Γ point in vdWH [Figs. 2(a)–2(c) and 2(e)]. The spin-up CB edges do not change their k -point location from subsystems to vdWH. The band alignments for the spin-up channel are sketched in Fig. 2(e) for both isolated subsystems and vdWH, which are derived from the band structures in Figs. 2(a)–2(c).

The valence and conduction band offset sizes [VBO and CBO labeled in Fig. 2(e)] in isolated subsystems and in vdWH are summarized in Table II. The CBO from the isolated subsystems is 1.01 eV and that in vdWH is 0.85 eV. The VBO from the subsystems is 0.23 eV, and that in vdWH becomes zero due to the interlayer QB interaction and the resulting orbital mixing between the two layers. As a result, the spin-up band alignment forms a special type with zero VBO, which is at the critical point between type I and type II, and is called a type H heterojunction [78]. The novel band alignment and its transition nature enable this kind of vdW heterostructure to be used for applications in special optoelectronic devices and energy conversion [42]. Moreover, the interlayer mixed electronic structure and the band alignment types could be tuned between type I and type II by, for example, applying vertical external electric fields, in-plane strain, or changing the interlayer distance.

TABLE II. Magnitude of band offsets of spin-up and spin-down from band edges in isolated subsystems and from those in vdWH. CBO (VBO) is the conduction (valence) band offset.

Band offset sizes (eV)		Isolated systems	vdWH
Spin-up	CBO	1.01	0.85
	VBO	0.23	0
Spin-down	CBO	1.39	1.28
	VBO	0.47	0.35

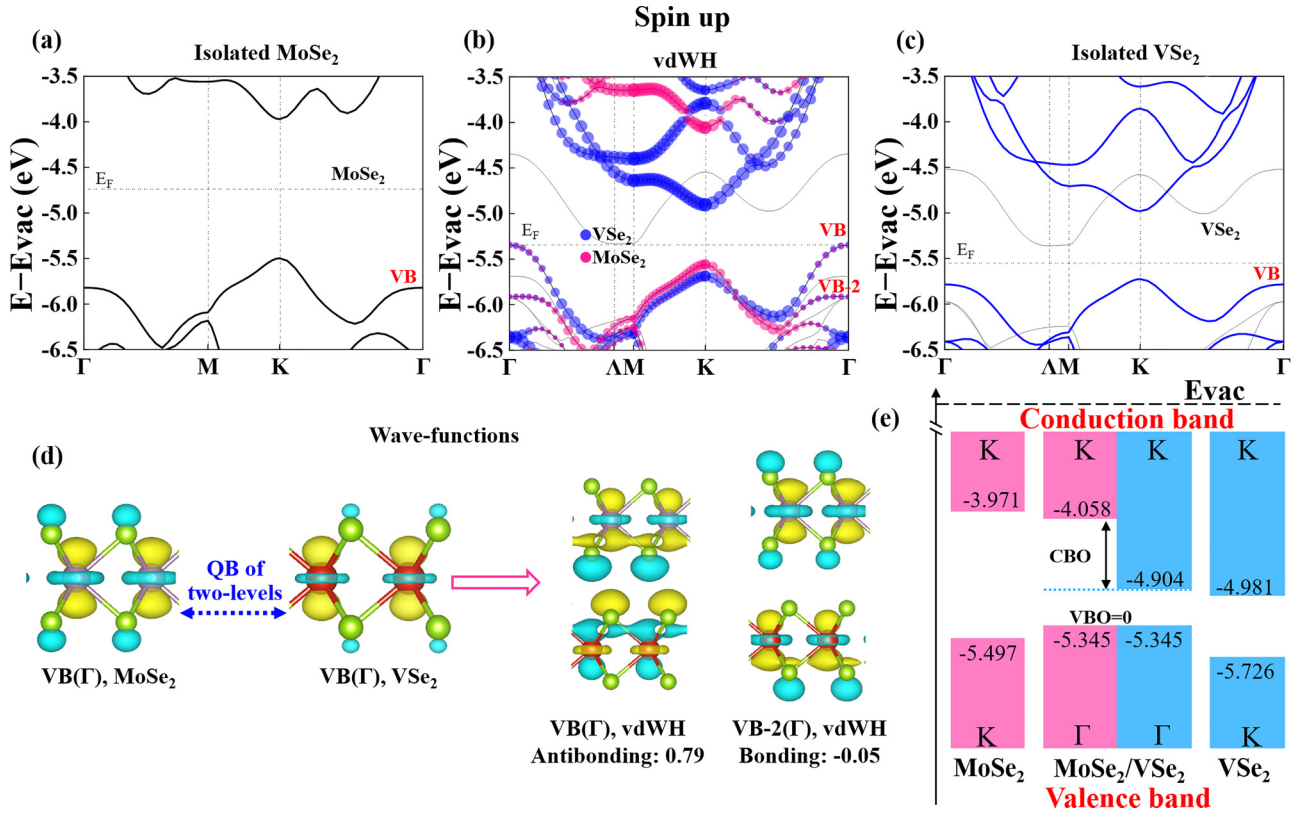


FIG. 2. Spin-up: interlayer orbital mixing and type H band alignment. (a–c) Band structure of the isolated MoSe₂, VSe₂ subsystems and the layer-projected band structure of vdWH. The bands from the other spin (spin-down) are denoted with light gray, thinner lines. In (b), the dot sizes indicate the magnitude of projection. (d) Wave functions at the Γ point of the VBs from the two isolated subsystems (MoSe₂, VSe₂) to the VB and VB-2 in vdWH; the VBs and VB-2 are also labeled in panels (a–c). The two colors of wave function denote the opposite signs; the relative strength of *interlayer* antibonding (bonding) interactions in VB (VB-2) of vdWH are indicated by the COHP numbers (0.79 and -0.05) in panel (d) and a positive (negative) number means bonding (antibonding), which is from the values of “Sum of ALL” in Table I. (e) Band alignment diagram for the spin-up channel; the VBO is zero due to interlayer orbital mixing and the type H band alignment is formed.

In Fig. 2(d), the wave function of VB in vdWH further indicates that the interlayer orbital hybridization is mainly the p_z orbital of interfacial Se atoms. Figure S7(a) [59] shows the band structure projected to p_z and the projection to other orbitals in Figs. S7(b)–S7(f) [59]. From the vdWH VB wave function in Fig. 2(d), it can be seen that the VB has interlayer-antibonding character, which is in line with the projected-COHP analysis (Table I).

C. Spin-down and interlayer three-level interaction

For spin-down, Figs. 3(a) and 3(c) show the band structures of the subsystems MoSe₂ and VSe₂ and Fig. 3(b) shows the layer-projected band structure of the vdWH. The vdWH VB-1 comes mainly from MoSe₂ and the vdWH CB comes mainly from VSe₂ [refer to Figs. 3(b) and 3(d)]. The CB edge of vdWH does not change their k -point location in the Brillouin zone relative to that in the subsystem, due to the energy mismatch between subsystem MoSe₂ VB and VSe₂ CB [Figs. 3(a), 3(c), and 1(e)], which results in the weaker interlayer interaction for CB. The formation of VB-1 in vdWH is a bit more complicated as will be detailed later. The type II band alignment for the spin-down channel is sketched in Fig. 3(e) and the band offset sizes are summarized in Table II.

Unlike the two-level interaction for the spin-up channel, the interlayer interaction for spin-down is a three-level interaction since the VSe₂ spin-down levels shift up in energy due to exchange splitting. As shown in Figs. 1(e), 1(i), and 3(d), the VB level of MoSe₂ at the Γ point hybridizes with the CB and VB-5 levels of VSe₂ that have the Se- p_z orbital character. The wave function at the Γ point of CB and VB-5 of spin-down for the subsystem VSe₂ is shown in Fig. 3(d). The vdWH wave function of CB(Γ) and VB-1(Γ) [refer to Fig. 3(b) for the labeled CB and VB-1] is also shown in Fig. 3(d). The wave functions show obvious p_z orbital antibonding interactions across the vdW gap. The band structure projected to the p_z orbital is shown in Fig. S7(i) [59] and the projection to other orbitals is also given in the other panels of Figs. S7(g)–S7(l) [59].

In addition to the above-mentioned energy upshift of VB-1 in vdWH relative to the VB in MoSe₂ at the Γ point [refer to Figs. 1(e), 3(a), and 3(b)], for the vdWH wave functions (VB-1 and CB of vdWH) in Fig. 3(d), there are two features that cannot be understood if assuming a two-level interaction between MoSe₂ VB and VSe₂ CB:

(1) One is the appearance of two consecutive interlayer-antibonding levels of CB and VB-1: as expected, the CB(Γ) of vdWH is antibonding at the vdWH interface; however, the VB-1(Γ) of vdWH is also interlayer antibonding.

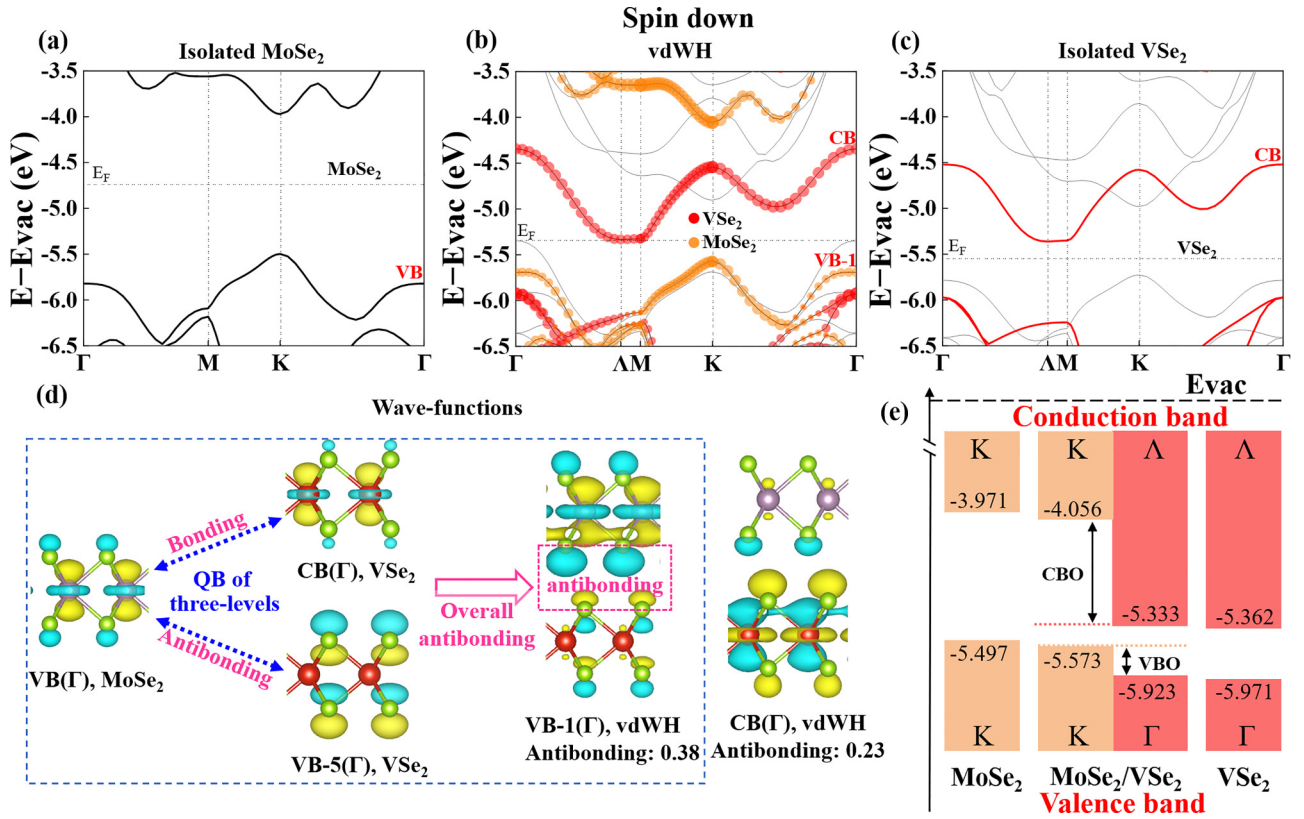


FIG. 3. Spin-down: three-level interaction and type II band alignment. (a–c) band structure of the isolated MoSe₂, VSe₂ subsystems and the layer-projected band structure of vdWH. The bands from the other spin (spin-up) are denoted with light gray lines. The dot sizes indicate the magnitude of projection. (d) Spin-down wave functions from isolated subsystems (VB of MoSe₂, CB and VB-5 of VSe₂) to CB and VB-1 in vdWH, and an illustration to the antibonding state formation of VB-1(Γ) in vdWH. The VB of MoSe₂ and CB and VB-5 of VSe₂ are also labeled in panels (a,c) and Fig. 1(i); VB-1 and CB of vdWH are also labeled in panel (b). The two colors of wave functions denote the opposite signs. The relative strength of *interlayer* antibonding interactions in VB-1 and CB of vdWH are indicated by the COHP numbers (0.38 and 0.23) in panel (d) and a positive number means bonding; these are from the values of “Sum of ALL” in Table I. (e) Type II band alignment for the spin-down channel.

(2) The other feature is the VB-1(Γ) wave function of vdWH at the lower VSe₂ part [see Fig. 3(d)]: it is not simply from the CB(Γ) of the isolated VSe₂, but is a combination of the VB-5(Γ) and CB(Γ) of isolated VSe₂, with the Se- p_z orbital character from VB-5(Γ) and the V- d_{z^2} orbital character from CB(Γ) of the isolated VSe₂ (with different weights for the two VSe₂ levels).

The vdWH VB-1 wave function in Fig. 3(d) becomes understandable by introducing a deeper VSe₂ level for the interlayer interaction, namely, the VB-5(Γ) of isolated VSe₂ with the Se- p_z orbital character [also refer to Fig. 1(i)], which makes the VB-1(Γ) of vdWH become antibonding [Fig. 1(e)]. The COHP analysis in Table I confirms the antibonding character of VB-1(Γ).

Moreover, we quantify the contributions of the VB-5 and CB of VSe₂ to the VB-1 of vdWH in Table III. Table III lists the projections of the vdWH VB-1 wave functions at the Γ point onto cubic harmonics of the V and Se atoms of VSe₂, and the Mo atom of MoSe₂. From the subsystem wave functions in Fig. 3(d), it is apparent that the MoSe₂ VB is dominated by the Mo- d_{z^2} orbital, and the CB(Γ) and VB-5(Γ) of VSe₂ are dominated by the V- d_{z^2} and Se- p_z orbital, respectively. As a result, for the contributions of subsystems to the vdWH VB-1(Γ), the projection to Mo- d_{z^2} (of 0.486)

roughly represents the contribution of the subsystem MoSe₂ VB to the vdWH, and the projection of V- d_{z^2} (0.033) and Se- p_z (0.031) roughly represent the contributions of CB(Γ) and VB-5(Γ) of VSe₂ to vdWH, respectively. Although the weights of CB(Γ) and VB-5(Γ) of VSe₂ are similar (0.033 vs 0.031), the interface Se atom is closer to the vdW gap than the V atom, so the effect of Se- p_z is stronger than that of V- d_{z^2} for interlayer interaction (also note that the orbital radius of Se- p is larger than V- d). This means that the effect of VB-5(Γ) is stronger than that of CB(Γ), and results in the overall interlayer-antibonding character in the VB-1 wave function of vdWH.

Figure 3(e) displays the type II band alignment for the spin-down channel. In vdWH, the CBO is 1.28 eV and the VBO

TABLE III. The projections of VB-1 wave functions of vdWH at the Γ point onto cubic harmonics of the V and Se atoms of VSe₂, and the Mo atom of MoSe₂.

	VB-1(Γ) of vdWH
VSe ₂	V- d_{z^2} : 0.033 (CB) Se- p_z : 0.031 (VB-5)
MoSe ₂	Mo- d_{z^2} : 0.486 (VB)

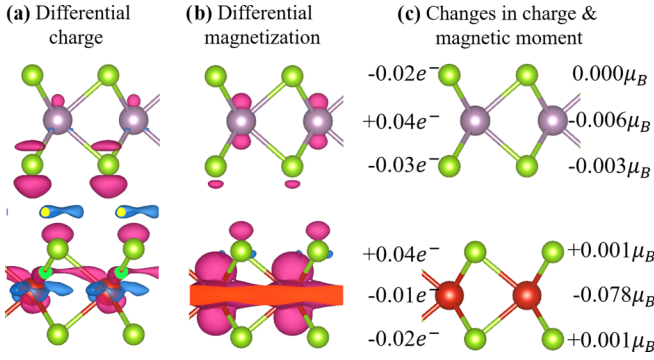


FIG. 4. Differential charge/magnetization densities (a,b) and changes in charge/magnetic moment (c) of vdWH relative to that of subsystems. (a) Differential charge and (b) differential magnetization densities. Blue and red denote accumulation and depletion, respectively. The same isosurface of $3 \times 10^{-4} e^-/a_0^3$ is used for the plots. (c) The labeled numbers are the changes in charge/magnetic moment on each atom of vdWH relative to that in subsystems based on Bader charge analysis. The Bader charge and “Bader magnetization” are obtained by summing the charge/magnetization densities in the atomic Bader volumes, and the Bader volume is determined by the total charge.

is 0.35 eV. From the subsystems to vdWH, both CBO and VBO are decreased by ~ 0.1 eV, as shown in Table II. We have checked that the inclusion of spin-orbit coupling (SOC) does not change our main conclusion for band alignment (Fig. S8 [59]).

Differential charge and magnetization. Interface QB not only results in energy-level reconstruction in energy and in the valley, but also leads to charge redistribution [79] and spin/magnetization redistribution. Figures 4(a) and 4(b) show the differential charge/magnetization densities from subsystems to vdWH. The differential charge/magnetization densities display their redistributions in real space, which is the integration for all occupied states (while for the QB discussions above, one usually focuses on the energy levels close to the Fermi level). Figure 4(a) exhibits the electron accumulation at the MoSe₂/VSe₂ vdW interface, which is a typical feature of interlayer QB formation [17]; also see Fig. 5(a) for the plane-averaged differential charge density along the

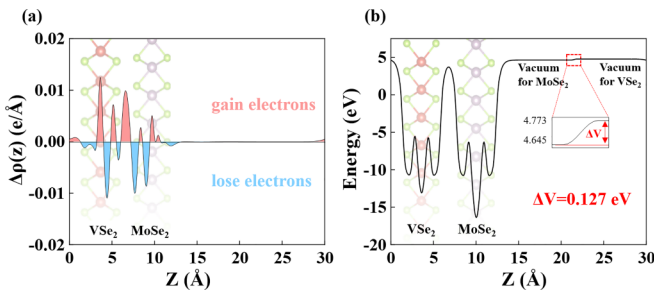


FIG. 5. Charge redistribution and interface dipole. (a) Plane-averaged differential charge density along the z direction normal to the MoSe₂/VSe₂ vdWH interface. (b) Plane-averaged electric potential and the interface potential step, ΔV , for the MoSe₂/VSe₂ vdWH.

z direction normal to the vdWH interface. The differential magnetization density in Fig. 4(b) shows that magnetization is induced on the Mo atom and the Se atom close to the vdWH interface. The labeled numbers in Fig. 4(c) quantify the charge transfer and magnetic moment change on the metal and Se atoms from isolated subsystems to vdWH, which are obtained by summing the differential charge/magnetization densities in the atomic Bader volumes for atoms in vdWH [80,81].

D. Quantify the effects of QB

As discussed above, the band offsets (VBO and CBO) change from isolated subsystems to vdWH (Table II). In vdWH, both interface QB (Δ_{QB}) and interface dipole (ΔV) affect band offsets, which are given by the following equations:

$$\text{CBO} = \text{CBO}_{\text{AR}} + \Delta V + \Delta_{\text{QB}}(\text{CB}), \quad (1)$$

$$\text{VBO} = \text{VBO}_{\text{AR}} + \Delta V + \Delta_{\text{QB}}(\text{VB}), \quad (2)$$

where the subscript AR means the band offset from isolated subsystems is given by Anderson’s rule [82]. The charge redistributions around the interface [Fig. 5(a)] lead to the formation of interface electric dipoles, ΔV , and interface potential steps at the vdWH interface. The ΔV is 0.127 eV in our vdWH, as shown in Fig. 5(b). The ΔV makes the vacuum levels different on the MoSe₂ and VSe₂ sides [83]; namely, two vacuum levels appear in the vdWH. For the band alignments in vdWH, Figs. 2(b), 2(e), 3(b), and 3(e), the averaged vacuum level is set to zero. The ΔV makes the band structure (VB and CB edges) of MoSe₂ shift downwards by 0.127 eV relative to that of VSe₂. The $\Delta_{\text{QB}}(\text{CB})$ and $\Delta_{\text{QB}}(\text{VB})$ are corrections for CBO and VBO from the interface QB effect, respectively, which is spin, band, and valley dependent as illustrated in the equations below.

From isolated subsystems to vdWH, $\Delta_{\text{QB}}(\text{CB})$ and $\Delta_{\text{QB}}(\text{VB})$ can be quantified from the QB induced relative changes of band edges at the MoSe₂ and VSe₂ sides, namely, $\Delta_{\text{QB}}(\text{VSe}_2) - \Delta_{\text{QB}}(\text{MoSe}_2)$, where $\Delta_{\text{QB}}(\text{VSe}_2)$ and $\Delta_{\text{QB}}(\text{MoSe}_2)$ are the QB induced band edges changes in the VSe₂ and MoSe₂ layers, respectively.

For spin-up [refer to Fig. 2(e)], they are

$$\begin{aligned} \Delta_{\text{QB}}(\text{CB}, \text{up}) &= \Delta_{\text{QB}}(\text{CB}, \text{up}, \text{VSe}_2) \\ &\quad - \Delta_{\text{QB}}(\text{CB}, \text{up}, \text{MoSe}_2) \approx 0.01 + 0.02 \\ &= 0.03 \text{ eV}, \end{aligned} \quad (3)$$

$$\begin{aligned} \Delta_{\text{QB}}(\text{VB}, \text{up}) &= \Delta_{\text{QB}}(\text{VB}, \text{up}, \text{VSe}_2) \\ &\quad - \Delta_{\text{QB}}(\text{VB}, \text{up}, \text{MoSe}_2) \approx 0.32 - 0.22 \\ &= 0.10 \text{ eV}. \end{aligned} \quad (4)$$

Note that in Fig. 2(e), the possible valley changes due to interlayer QB interaction, from the K point to the Γ point for valence band edges, are already included.

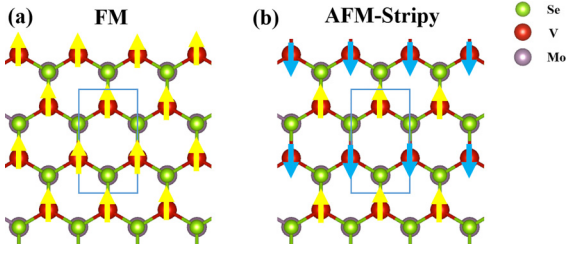


FIG. 6. The FM and AFM magnetic ordering of the $H\text{-MoSe}_2/H\text{-VSe}_2$ heterostructure. The rectangles indicate the supercell used. Note that here we used an area-doubled ($1 \times \sqrt{3}$) rectangular supercell for the possible AFM configuration(s). There is only one inequivalent AFM configuration for both ($1 \times \sqrt{3}$) rectangular and $p(2 \times 2)$ supercells for a triangular magnetic lattice [87].

For spin-down [refer to Fig. 3(e)], they are

$$\begin{aligned} \Delta_{\text{QB}}(\text{CB, down}) &= \Delta_{\text{QB}}(\text{CB, down, VSe}_2) \\ &\quad - \Delta_{\text{QB}}(\text{CB, down, MoSe}_2) \approx 0.03 - 0.02 \\ &= 0.01 \text{ eV}, \end{aligned} \quad (5)$$

$$\begin{aligned} \Delta_{\text{QB}}(\text{VB, down}) &= \Delta_{\text{QB}}(\text{VB, down, VSe}_2) \\ &\quad - \Delta_{\text{QB}}(\text{VB, down, MoSe}_2) \approx 0.01 - 0.01 \\ &= 0 \text{ eV}. \end{aligned} \quad (6)$$

These numbers indicate that the QB induced band offset changes; namely, the Δ_{QB} 's for VB/CB and for spin-up/down, can be different for the different spin channel and different for VB and CB, and the value of Δ_{QB} ranges from 0 to 0.1 eV for our vdWH. In addition the QB effect of spin-up is stronger than that of spin-down.

E. Magnetism and potential applications

Magnetism. H -phase VSe_2 has a ferromagnetic ground state with an in-plane easy axis [48]. To study the magnetic properties of VSe_2 from monolayer to those in the $H\text{-MoSe}_2/H\text{-VSe}_2$ heterostructure, we employ a ($1 \times \sqrt{3}$) rectangular supercell (Fig. 6). Table IV shows that the exchange energy ($E_{\text{ex}} = E_{\text{FM}} - E_{\text{AFM}}$) per vanadium atom is negative, which indicates the ferromagnetic ground state; this conclusion is consistent with that in the literature [84–86]. The magnetic anisotropy energy (MAE) is calculated as the energy difference between magnetization along the in-plane and out of plane directions: $\text{MAE} = E_{\text{in plane}} - E_{\text{out of plane}}$ [85,86]. A negative MAE represents the in-plane easy axis. As shown in Table IV, for VSe_2 coupling with MoSe_2 in vdWH, the mag-

TABLE IV. The magnetic anisotropy energy (MAE), nearest-neighbor exchange parameter (J_1), and Curie temperature (T_C) of monolayer VSe_2 and VSe_2 in the van der Waals heterostructure (vdWH). All energies are per vanadium atom.

H phase	MAE (meV)	J_1 (meV)	T_C (K)
Monolayer VSe_2	-0.72	-25.43	423
VSe_2 in vdWH	-0.68	-22.78	376

netic ground state of the VSe_2 layer remains ferromagnetic and in-plane easy axis.

To obtain the nearest-neighbor exchange parameter (J_1), we use the two magnetic configurations as shown in Fig. 6. The total energy of the FM state is expressed as $E_{\text{FM}} = -6J_1 + E_0$, on account of three FM coupling interactions in one unit cell, where E_0 is the energy independent of magnetic order. Because of two AFM and one FM coupling interactions in one unit cell of the AFM state, the total energy of the AFM state is expressed as $E_{\text{AFM}} = 2J_1 + E_0$. We estimate the Curie temperature (T_C) by Monte Carlo simulations of the Heisenberg model with a magnetic anisotropy term [88]. The spin Hamiltonian with a magnetic anisotropy term is described as

$$H = -J \sum_{i,j} \mathbf{S}_i \cdot \mathbf{S}_j - A \sum_i (S_i^z)^2$$

where i, j is the nearest-neighbor unit cell site, J is the nearest-neighbor exchange parameter, \mathbf{S} is the unit vector representing the direction of the magnetic moment, and A is the magnetic anisotropy energy. We adopted the Monte Carlo simulations for the magnetizations as functions of the temperature to calculate the Curie temperature. Figure S11 [59] shows that the Curie temperature is around 423 K for monolayer VSe_2 and 376 K for VSe_2 in vdWH (more details can be found in the Supplemental Material [59]). The results are summarized in Table IV. From all the magnetic properties in Table IV, one sees that the original magnetic properties of $H\text{-VSe}_2$ monolayer are largely maintained in the $H\text{-MoSe}_2/H\text{-VSe}_2$ vdWH.

Band alignment. As discussed above, due to the spin-dependent interlayer QB effect, the properties of the vdWH for spin-up and spin-down are different. The characteristics of the vdWH mainly depend on the band-edge alignments in energy and valley [89–91]. Generally speaking, 2D vdWHs are classified into three main categories: type I (straddling gap), type II (staggered gap), and type III (broken gap) [92,93], which have wide applications for the understanding of the basic photoprocesses as well as for the control of efficiency in charge transfer at the interface. The band alignment types for the two spin channels are different in the $\text{MoSe}_2/\text{VSe}_2$ vdWH and hence the vdWH can have multiple applications by using the different band alignments for the two spin channels [7,77].

For the band alignment of the spin-up channel, we find in the above that the interlayer QB mixing can induce the $\text{MoSe}_2/\text{VSe}_2$ vdWH to exhibit a special type of band alignment with zero VBO [Fig. 2(e)], namely, the type H at the critical point between type I and type II [78].

On the other hand, the VB at the Γ point can be considered as mainly on the VSe_2 layer since the contribution from VSe_2 is a bit larger; the ratio is 4:3 for the contributions from VSe_2 and MoSe_2 layers. This results in the type I band alignment in Fig. S9 [59]. The VB edge of VSe_2 changes from the K to the Γ point from isolated VSe_2 to VSe_2 in vdWH, and the other band edges remain at the K point. It should be noted that the QB-mixing effect frequently appears in vdWHs of 2D semiconductors, and the band alignments were classified either as type II/I [94] or type H [78] in the literature for different applications.

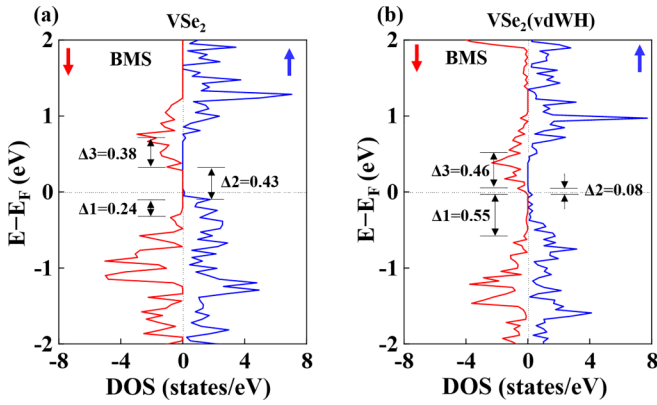


FIG. 7. The BMS properties from spin-polarized density of states of (a) monolayer VSe_2 and (b) VSe_2 in vdWH. The three energy gaps $\Delta 1$, $\Delta 2$, and $\Delta 3$ for the BMS performance are labeled. Blue and yellow denote spin-up and spin-down, respectively.

So, the spin-up channel of the $MoSe_2/VSe_2$ vdWH can exhibit two types of band alignments for different applications: type *H* and type *I* alignments. The novel band alignment and transition properties make the $MoSe_2/VSe_2$ vdWH applicable in special optoelectronic devices and energy conversion [42] for spin-dependent (opto)electronics [7] and photoelectric devices [77]. Moreover, the spin-down $MoSe_2/VSe_2$ vdWH exhibits a type *II* band alignment, which broadens the possible application.

Bipolar magnetic semiconductors. Magnetic semiconductors combine the advantages of magnetic materials and semiconductor materials, which are the basis for their use as spin channel materials. Magnetic semiconductors can generate, inject, control, and detect electronic spin, and, can be easily applied to current semiconductor technology [95]. According to their different electronic and magnetic properties, magnetic semiconductors can be classified into half semiconductor, spin gapless semiconductor, bipolar magnetic semiconductor (BMS), and asymmetric antiferromagnetic semiconductor [95]. Among them, BMS has a unique electronic structure [Fig. 7(a)]: its VBM and CBM are completely spin polarized and have opposite polarization directions. For the performance of a BMS, one can use three band gaps to describe the unique electronic structure, that is, two band gaps located in the valence band or conduction band that can flip the spin ($\Delta 1$ and $\Delta 3$) as well as the band gap that needs to be overcome for electron transport ($\Delta 2$). These three types of gaps are labeled in Fig. 7.

The interlayer QB effect in the $MoSe_2/VSe_2$ vdWH is spin dependent (spin-up is stronger than spin-down), which results in the changes in the three types of gaps. In particular, the valence band edge of VSe_2 in vdWH shifts up in energy compared to that of monolayer VSe_2 , resulting in significant changes in the gaps of $\Delta 2$ and $\Delta 1$. It can be seen in Fig. 7 that from monolayer VSe_2 to VSe_2 in vdWH, the band gap $\Delta 2$ decreases by 0.35 eV (from 0.43 to 0.08 eV), the spin-flip gap $\Delta 1$ increases by 0.31 eV (from 0.24 to 0.55 eV) and $\Delta 3$ increases by 0.08 eV (from 0.38 to 0.46 eV). For spintronic applications, it is better to have larger spin-flip gaps ($\Delta 1$ and $\Delta 3$) and smaller transport gap ($\Delta 2$). From monolayer VSe_2 to

VSe_2 in vdWH, the transport gap $\Delta 2$ decreases and both of the spin-flip gaps $\Delta 1$ and $\Delta 3$ increase. So, the formation of vdWH with $MoSe_2$ makes the BMS properties better in VSe_2 .

In summary, for potential applications, the spin-polarized $MoSe_2/VSe_2$ vdWH exhibits different band alignments for the two spin channels and the interlayer QB-mixing effect could make a special type *H* band alignment for the spin-up channel. For spintronic applications, the QB in vdWH improves the BMS properties in the VSe_2 layer. As a result, the $MoSe_2/VSe_2$ vdWH has the potential to be used as a multifunctional heterostructure for spintronics and spin-dependent optoelectronics.

IV. CONCLUSIONS AND REMARKS

In conclusion, the spin-dependent interlayer QB interaction induces spin polarization on $MoSe_2$ and the intrinsic magnetic properties on VSe_2 are largely maintained in vdWH. The two-level interlayer QB interaction for spin-up is different from the three-level QB interaction for spin-down. The spin-dependent interlayer QB interaction in the $MoSe_2/VSe_2$ vdWH influences the band alignment, and its applications in spin-dependent optoelectronics and spintronics are discussed. The spin-up channel exhibits the characteristics of type *H* and type *I* band alignments, while the spin-down channel behaves as a type *II* heterostructure. For spintronics application, the interlayer QB increases the spin-flip gap and reduces the transport gap of VSe_2 , and hence improves its BMS performance. All the above indicates that the $MoSe_2/VSe_2$ vdWH has multifunctional properties and has potentials for spin-dependent optoelectronics and spintronics.

Although we focus on the Γ point in the current work since at the Γ point the interface orbital hybridization is much stronger than at the K point, the orbital-resolved analysis used here can also be applied to the K point and may provide a deep understanding of the recently reported asymmetric magnetic proximity interactions between the K and K' points [7,8]. The recent literature [96–99] also shows that the Γ -valley (but not the K -valley) flat bands are involved in the correlated physics of twisted group-VI TMDs. The orbital-resolved multilevel analysis here can be seen as a powerful tool for understanding the fundamental physics of interlayer interaction that contains different interlayer interaction types that the occupied-occupied and occupied-empty interactions coexistence [14], such as in black phosphorus and InSe [100,101].

ACKNOWLEDGMENTS

This work was supported by the National Natural Science Foundation of China (Grants No. 12274111 and No. 12104124), the Natural Science Foundation of Hebei Province of China (Grants No. A2021201001 and No. A2021201008), the Scientific Research and Innovation Team of Hebei University (Grant No. IT2023B03), the Advanced Talents Incubation Program of Hebei University (Grants No. 521000981390, No. 521000981394, No. 521000981395, No. 521000981423, and No. 521100221055), and the high-performance computing center of Hebei University.

- [1] J. H. Kang, W. Liu, D. Sarkar, D. Jena, and K. Banerjee, Computational study of metal contacts to monolayer transition-metal dichalcogenide semiconductors, *Phys. Rev. X* **4**, 031005 (2014).
- [2] I. Popov, G. Seifert, and D. Tomanek, Designing electrical contacts to MoS₂ monolayers: A computational study, *Phys. Rev. Lett.* **108**, 156802 (2012).
- [3] Q. H. Wang, K. Kalantar-Zadeh, A. Kis, J. N. Coleman, and M. S. Strano, Electronics and optoelectronics of two-dimensional transition metal dichalcogenides, *Nat. Nanotechnol.* **7**, 699 (2012).
- [4] T. Shen, J. C. Ren, X. Liu, S. Li, and W. Liu, Van der Waals stacking induced transition from Schottky to ohmic contacts: 2D metals on multilayer InSe, *J. Am. Chem. Soc.* **141**, 3110 (2019).
- [5] W. Q. Liu, W. Y. Wang, J. J. Wang, F. Q. Wang, C. Lu, F. Jin, A. Zhang, Q. M. Zhang, G. V. Laan, Y. B. Xu *et al.*, Atomic-scale interfacial magnetism in Fe/Graphene heterojunction, *Sci. Rep.* **5**, 11911 (2015).
- [6] A. M. Hoque, D. Khokhriakov, B. Karpiak, and S. P. Dash, Charge-spin conversion in layered semimetal TaTe₂ and spin injection in van der Waals heterostructures, *Phys. Rev. Res.* **2**, 033204 (2020).
- [7] J. Choi, C. Lane, J. X. Zhu, and S. A. Crooker, Asymmetric magnetic proximity interactions in MoSe₂/CrBr₃ van der Waals heterostructures, *Nat. Mater.* **22**, 305 (2023).
- [8] D. Wang and X. Zou, Tunable valley band and exciton splitting by interlayer orbital hybridization, *npj Comput. Mater.* **8**, 239 (2022).
- [9] M. H. Naik and M. Jain, Ultraflatbands and shear solitons in moiré patterns of twisted bilayer transition metal dichalcogenides, *Phys. Rev. Lett.* **121**, 266401 (2018).
- [10] G. Di Liberto, L. A. Cipriano, S. Tosoni, and G. Pacchioni, Rational design of semiconductor heterojunctions for photocatalysis, *Chem.* **27**, 13306 (2021).
- [11] J. H. Zhang, M. S. Deng, Y. A. Yan, T. J. Xiao, W. Ren, and P. H. Zhang, Tunable type-II BiVO₄/g-C₃N₄ nanoheterostructures for photocatalysis applications, *Phys. Rev. Appl.* **11**, 044052 (2019).
- [12] J. Klimes and A. Michaelides, Perspective: Advances and challenges in treating van der Waals dispersion forces in density functional theory, *J. Chem. Phys.* **137**, 120901 (2012).
- [13] Y. Zhao, J. Qiao, P. Yu, Z. Hu, Z. Lin, S. P. Lau, Z. Liu, W. Ji, and Y. Chai, Extraordinarily strong interlayer interaction in 2D layered PtS₂, *Adv. Mater.* **28**, 2399 (2016).
- [14] Y. T. Chen, P. L. Gong, Y. T. Ren, L. Hu, H. Zhang, J. L. Wang, L. Huang, and X. Q. Shi, Interlayer quasi-bonding interactions in 2D layered materials: A classification according to the occupancy of involved energy bands, *J. Phys. Chem. Lett.* **12**, 11998 (2021).
- [15] Y. Huang, Y. H. Pan, R. Yang, L. H. Bao, L. Meng, H. L. Luo, Y. Q. Cai, G. D. Liu, W. J. Zhao, Z. Zhou *et al.*, Universal mechanical exfoliation of large-area 2D crystals, *Nat. Commun.* **11**, 2453 (2020).
- [16] Z. Bian, J. Miao, Y. Zhao, and Y. Chai, Strong interlayer interaction for engineering two-dimensional materials, *Acc. Mater. Res.* **3**, 1220 (2022).
- [17] H. Kasai, K. Tolborg, M. Sist, J. Zhang, V. R. Hathwar, M. O. Filso, S. Cenedese, K. Sugimoto, J. Overgaard, E. Nishibori *et al.*, X-ray electron density investigation of chemical bonding in van der Waals materials, *Nat. Mater.* **17**, 249 (2018).
- [18] D. Jariwala, T. J. Marks, and M. C. Hersam, Mixed-dimensional van der Waals heterostructures, *Nat. Mater.* **16**, 170 (2017).
- [19] L. X. Zhou, Y. T. Ren, Y. T. Chen, X. H. Lv, C. D. Jin, H. Zhang, P. L. Gong, R. Q. Lian, R. N. Wang, J. L. Wang *et al.*, Quasi-bonding-induced gap states in metal/two-dimensional semiconductor junctions: Route for Schottky barrier height reduction, *Phys. Rev. B* **105**, 224105 (2022).
- [20] Á. Szabó, R. Rhyner, and M. Luisier, *Ab initio* simulation of single- and few-layer MoS₂ transistors: Effect of electron-phonon scattering, *Phys. Rev. B* **92**, 035435 (2015).
- [21] T. K. Maji, K. Vaibhav, S. K. Pal, K. Majumdar, K. V. Adarsh, and D. Karmakar, Intricate modulation of interlayer coupling at the graphene oxide/MoSe₂ interface: Application in time-dependent optics and device transport, *Phys. Rev. B* **99**, 115309 (2019).
- [22] L. Rogee, L. Wang, Y. Zhang, S. Cai, P. Wang, M. Chhowalla, W. Ji, and S. P. Lau, Ferroelectricity in untwisted heterobilayers of transition metal dichalcogenides, *Science* **376**, 973 (2022).
- [23] Z. X. Hu, X. Kong, J. Qiao, B. Normand, and W. Ji, Interlayer electronic hybridization leads to exceptional thickness-dependent vibrational properties in few-layer black phosphorus, *Nanoscale* **8**, 2740 (2016).
- [24] C. Wang, X. Zhou, L. Zhou, Y. Pan, Z.-Y. Lu, X. Wan, X. Wang, and W. Ji, Bethe-Slater-curve-like behavior and interlayer spin-exchange coupling mechanisms in two-dimensional magnetic bilayers, *Phys. Rev. B* **102**, 020402(R) (2020).
- [25] W. Chen, Z. Sun, Z. Wang, L. Gu, X. Xu, S. Wu, and C. Gao, Direct observation of van der Waals stacking-dependent interlayer magnetism, *Science* **366**, 983 (2019).
- [26] P. H. Jiang, C. Wang, D. C. Chen, Z. C. Zhong, Z. Yuan, Z. Y. Lu, and W. Ji, Stacking tunable interlayer magnetism in bilayer CrI₃, *Phys. Rev. B* **99**, 144401 (2019).
- [27] S. Mohanty, W. Gao, and P. Deb, Augmented and quenched local moments in a van der Waals itinerant moiré ferromagnet, *Phys. Rev. B* **108**, 054433 (2023).
- [28] S. Mohanty and P. Deb, Nontrivial band topology coupled thermoelectrics in VSe₂/MoSe₂ van der Waals magnetic Weyl semimetal, *J. Phys.: Condens. Matter* **34**, 335801 (2022).
- [29] J. W. Chen, T. Zhang, J. L. Wang, N. Zhang, W. Ji, S. Y. Zhou, and Y. Chai, Field-effect chiral anomaly devices with Dirac semimetal, *Adv. Funct. Mater.* **31**, 2104192 (2021).
- [30] J. Qiao, X. Kong, Z. X. Hu, F. Yang, and W. Ji, High-mobility transport anisotropy and linear dichroism in few-layer black phosphorus, *Nat. Commun.* **5**, 4475 (2014).
- [31] J. Yang, R. J. Xu, J. J. Pei, Y. W. Myint, F. Wang, Z. Wang, S. Zhang, Z. F. Yu, and Y. R. Lu, Optical tuning of exciton and trion emissions in monolayer phosphorene, *Light: Sci. Appl.* **4**, e312 (2015).
- [32] Y.-T. Ren, Y.-T. Chen, L. Hu, J.-L. Wang, P.-L. Gong, H. Zhang, L. Huang, and X.-Q. Shi, *p*-Type ohmic contact to MoS₂ via binary compound electrodes, *J. Mater. Chem. C* **11**, 3119 (2023).
- [33] F. H. Davies, C. J. Price, N. T. Taylor, S. G. Davies, and S. P. Hepplestone, Band alignment of transition metal dichalcogenide heterostructures, *Phys. Rev. B* **103**, 045417 (2021).

- [34] Y.-J. Zhang, Y.-T. Ren, X.-H. Lv, X.-L. Zhao, R. Yang, N.-W. Wang, C.-D. Jin, H. Zhang, R.-Q. Lian, P.-L. Gong *et al.*, Momentum matching and band-alignment type in van der Waals heterostructures: Interfacial effects and materials screening, *Phys. Rev. B* **107**, 235420 (2023).
- [35] Y. Ozguven, H. E. Guler, A. A. Billur, A. Mogulkoc, and M. Modarresi, Robust ferromagnetism in two-dimensional GeC/CrN heterobilayers, *Phys. Chem. Chem. Phys.* **25**, 22370 (2023).
- [36] M. Modarresi, A. Mogulkoc, Y. Mogulkoc, and A. N. Rudenko, lateral spin valve based on the two-dimensional CrN/P/CrN heterostructure, *Phys. Rev. Appl.* **11**, 064015 (2019).
- [37] J. Zhou, J. Qiao, C.-G. Duan, A. Bournel, K. L. Wang, and W. Zhao, Large tunneling magnetoresistance in VSe₂/MoS₂ magnetic tunnel junction, *ACS Appl. Mater. Interfaces* **11**, 17647 (2019).
- [38] W. Xiong, C. Xia, J. Du, T. Wang, X. Zhao, Y. Peng, Z. Wei, and J. Li, Electrostatic gating dependent multiple-band alignments in a high-temperature ferromagnetic Mg(OH)₂/VS₂ heterobilayer, *Phys. Rev. B* **95**, 245408 (2017).
- [39] N. Lu, H. Guo, L. Li, J. Dai, L. Wang, W.-N. Mei, X. Wu, and X. C. Zeng, MoS₂/MX₂ heterobilayers: Bandgap engineering via tensile strain or external electrical field, *Nanoscale* **6**, 2879 (2014).
- [40] I. Khan, J. Ahmad, M. E. Mazhar, and J. Hong, Strain tuning of the Curie temperature and valley polarization in two dimensional ferromagnetic WSe₂/CrSnSe₃ heterostructure, *Nanotechnology* **32**, 375708 (2021).
- [41] R. Nelson, C. Ertural, J. George, V. L. Deringer, G. Hautier, and R. Dronskowski, LOBSTER: Local orbital projections, atomic charges, and chemical-bonding analysis from projector-augmented-wave-based density-functional theory, *J. Comput. Chem.* **41**, 1931 (2020).
- [42] Y. Si, H. Y. Wu, J. C. Lian, W. Q. Huang, W. Y. Hu, and G. F. Huang, A design rule for two-dimensional van der Waals heterostructures with unconventional band alignments, *Phys. Chem. Chem. Phys.* **22**, 3037 (2020).
- [43] J. Hafner, *Ab-initio* simulations of materials using VASP: Density-functional theory and beyond, *J. Comput. Chem.* **29**, 2044 (2008).
- [44] G. Kresse and J. Furthmüller, Efficient iterative schemes for *ab initio* total-energy calculations using a plane-wave basis set, *Phys. Rev. B* **54**, 11169 (1996).
- [45] P. E. Blochl, Projector augmented-wave method, *Phys. Rev. B* **50**, 17953 (1994).
- [46] G. Kresse and D. Joubert, From ultrasoft pseudopotentials to the projector augmented-wave method, *Phys. Rev. B* **59**, 1758 (1999).
- [47] J. P. Perdew, K. Burke, and M. Ernzerhof, Generalized gradient approximation made simple, *Phys. Rev. Lett.* **77**, 3865 (1996).
- [48] S. J. Gong, C. Gong, Y. Y. Sun, W. Y. Tong, C. G. Duan, J. H. Chu, and X. Zhang, Electrically induced 2D half-metallic antiferromagnets and spin field effect transistors, *Proc. Natl. Acad. Sci. USA* **115**, 8511 (2018).
- [49] S. L. Dudarev, G. A. Botton, S. Y. Savrasov, C. J. Humphreys, and A. P. Sutton, Electron-energy-loss spectra and the structural stability of nickel oxide: An LSDA+*U* study, *Phys. Rev. B* **57**, 1505 (1998).
- [50] M. Dion, H. Rydberg, E. Schroder, D. C. Langreth, and B. I. Lundqvist, Van der Waals density functional for general geometries, *Phys. Rev. Lett.* **92**, 246401 (2004).
- [51] J. Klimeš, D. R. Bowler, and A. Michaelides, Van der Waals density functionals applied to solids, *Phys. Rev. B* **83**, 195131 (2011).
- [52] H. J. Monkhorst and J. D. Pack, Special points for Brillouin-zone integrations, *Phys. Rev. B* **13**, 5188 (1976).
- [53] S. Maintz, V. L. Deringer, A. L. Tchougreeff, and R. Dronskowski, Analytic projection from plane-wave and PAW wavefunctions and application to chemical-bonding analysis in solids, *J. Comput. Chem.* **34**, 2557 (2013).
- [54] V. L. Deringer, A. L. Tchougreeff, and R. Dronskowski, Crystal orbital Hamilton population (COHP) analysis as projected from plane-wave basis sets, *J. Phys. Chem. A* **115**, 5461 (2011).
- [55] S. Maintz, M. Esser, and R. Dronskowski, Efficient rotation of local basis functions using real spherical harmonics, *Acta Phys. Pol., B* **47**, 1165 (2016).
- [56] S. Maintz, V. L. Deringer, A. L. Tchougreeff, and R. Dronskowski, LOBSTER: A tool to extract chemical bonding from plane-wave based DFT, *J. Comput. Chem.* **37**, 1030 (2016).
- [57] R. Dronskowski and P. E. Blochl, Crystal orbital Hamilton populations (COHP): Energy-resolved visualization of chemical bonding in solids based on density-functional calculations, *J. Phys. Chem. C* **97**, 8617 (1993).
- [58] X. Sun, X. Li, J. Yang, J. Xi, R. Nelson, C. Ertural, R. Dronskowski, W. Liu, G. J. Snyder, D. J. Singh *et al.*, Achieving band convergence by tuning the bonding ionicity in *n*-type Mg₃Sb₂, *J. Comput. Chem.* **40**, 1693 (2019).
- [59] See Supplemental Material at <http://link.aps.org/supplemental/10.1103/PhysRevB.109.045420> for structural stacking configurations and their band structures; phonon spectrum; interlayer distance scanning; more projected band structures; more on projected COHP; details on projecting VB-1 to cubic harmonics; type I band alignment for the spin-up channel; summary of multilevel interactions for spin-down; details on Monte Carlo simulation; spin-dependent interlayer band coupling. The Supplemental Material also contains Refs. [60–73].
- [60] G. Kresse and J. Hafner, *Ab initio* molecular dynamics for liquid metals, *Phys. Rev. B* **47**, 558 (1993).
- [61] G. Kresse and J. Hafner, *Ab initio* molecular-dynamics simulation of the liquid-metal-amorphous-semiconductor transition in germanium, *Phys. Rev. B* **49**, 14251 (1994).
- [62] W. Yu, J. Li, T. S. Heng, Z. Wang, X. Zhao, X. Chi, W. Fu, I. Abdelwahab, J. Zhou, J. Dan *et al.*, Chemically exfoliated VSe₂ monolayers with room-temperature ferromagnetism, *Adv. Mater.* **31**, 1903779 (2019).
- [63] G. Kresse and B. J. Furthmüller, Efficiency of *ab-initio* total energy calculations for metals and semiconductors using a plane-wave basis set, *Comput. Mater. Sci.* **6**, 15 (1996).
- [64] B. Marfoua and J. Hong, Electric field-induced switching of anomalous Nernst conductivity in the 2D MoTe₂/VSe₂ heterostructure, *Phys. Chem. Chem. Phys.* **24**, 22523 (2022).
- [65] X. Wang, D. Li, Z. Li, C. Wu, G. Chen, and X. Cui, Ferromagnetism in 2D vanadium diselenide, *ACS Nano* **15**, 16236 (2021).

- [66] L. Liang and V. Meunier, First-principles Raman spectra of MoS₂, WS₂ and their heterostructures, *Nanoscale* **6**, 5394 (2014).
- [67] E. Torun, H. P. C. Miranda, A. Molina-Sánchez, and L. Wirtz, Interlayer and intralayer excitons in MoS₂/WS₂ and MoSe₂/WSe₂ heterobilayers, *Phys. Rev. B* **97**, 245427 (2018).
- [68] G. M. Dalpian, S.-H. Wei, X. G. Gong, A. J. R. da Silva, and A. Fazzio, Phenomenological band structure model of magnetic coupling in semiconductors, *Solid State Commun.* **138**, 353 (2006).
- [69] D. Wines, J. Tiihonen, K. Saritas, J. T. Krogel, and C. Ataca, A quantum Monte Carlo study of the structural, energetic, and magnetic properties of two-dimensional *H* and *T* phase VSe₂, *J. Phys. Chem. Lett.* **14**, 3553 (2023).
- [70] S. Memarzadeh, M. R. Roknabadi, M. Modarresi, A. Mogulkoc, and A. N. Rudenko, Role of charge doping and strain in the stabilization of in-plane ferromagnetism in monolayer VSe₂ at room temperature, *2D Mater.* **8**, 035022 (2021).
- [71] M. Bonilla, S. Kolekar, Y. Ma, H. C. Diaz, V. Kalappattil, R. Das, T. Eggers, H. R. Gutierrez, M.-H. Phan, and M. Batzill, Strong room-temperature ferromagnetism in VSe₂ monolayers on van der Waals substrates, *Nat. Nanotechnol.* **13**, 289 (2018).
- [72] J. Kang, L. Zhang, and S.-H. Wei, A unified understanding of the thickness-dependent bandgap transition in hexagonal two-dimensional semiconductors, *J. Phys. Chem. Lett.* **7**, 597 (2016).
- [73] A. A. Mostofi, J. R. Yates, Y.-S. Lee, I. Souza, D. Vanderbilt, and N. Marzari, wannier90: A tool for obtaining maximally-localised Wannier functions, *Comput. Phys. Commun.* **178**, 685 (2008).
- [74] V. Wang, N. Xu, J. C. Liu, G. Tang, and W. T. Geng, VASPKIT: A user-friendly interface facilitating high-throughput computing and analysis using VASP code, *Comput. Phys. Commun.* **267**, 108033 (2021).
- [75] J. You, J. Pan, S. L. Shang, X. Xu, Z. Liu, J. Li, H. Liu, T. Kang, M. Xu, S. Li *et al.*, Salt-assisted selective growth of *H*-phase monolayer VSe₂ with apparent hole transport behavior, *Nano Lett.* **22**, 10167 (2022).
- [76] T. Björkman, A. Gulans, A. V. Krasheninnikov, and R. M. Nieminen, Van der Waals bonding in layered compounds from advanced density-functional first-principles calculations, *Phys. Rev. Lett.* **108**, 235502 (2012).
- [77] Y. Gao, Q. Liu, Y. Zhu, X. Jiang, and J. Zhao, Magnetic field modulated photoelectric devices in ferromagnetic semiconductor CrXh (*X* = S/Se, *h* = Cl/Br/I) van der Waals heterojunctions, *Appl. Phys. Lett.* **119**, 032103 (2021).
- [78] C. C. Tho, S.-D. Guo, S.-J. Liang, W.-L. Ong, C. S. Lau, L. Cao, G. Wang, and Y. S. Ang, MA₂Z₄ family heterostructures: Promises and prospects, *Appl. Phys. Rev.* **10**, 041307 (2023).
- [79] Q. Wang, Y. Shao, and X. Shi, Mechanism of charge redistribution at the metal-semiconductor and semiconductor-semiconductor interfaces of metal-bilayer MoS₂ junctions, *J. Chem. Phys.* **152**, 244701 (2020).
- [80] M. Yu and D. R. Trinkle, Accurate and efficient algorithm for Bader charge integration, *J. Chem. Phys.* **134**, 064111 (2011).
- [81] W. Tang, E. Sanville, and G. Henkelman, A grid-based Bader analysis algorithm without lattice bias, *J. Phys.: Condens. Matter* **21**, 084204 (2009).
- [82] Y. Si, H. Y. Wu, K. Yang, J. C. Lian, T. Huang, W. Q. Huang, W. Y. Hu, and G. F. Huang, High-throughput computational design for 2D van der Waals functional heterostructures: Fragility of Anderson's rule and beyond, *Appl. Phys. Lett.* **119**, 043102 (2021).
- [83] M. Farmanbar and G. Brocks, First-principles study of van der Waals interactions and lattice mismatch at MoS₂/metal interfaces, *Phys. Rev. B* **93**, 085304 (2016).
- [84] M. Esters, R. G. Hennig, and D. C. Johnson, Dynamic instabilities in strongly correlated VSe₂ monolayers and bilayers, *Phys. Rev. B* **96**, 235147 (2017).
- [85] S. Feng and W. Mi, Strain and interlayer coupling tailored magnetic properties and valley splitting in layered ferrovalley 2H-VSe₂, *Appl. Surf. Sci.* **458**, 191 (2018).
- [86] H. Sheng, H. Long, G. Zou, D. Bai, J. Zhang, and J. Wang, Magnetic and phonon transport properties of two-dimensional room-temperature ferromagnet VSe₂, *J. Mater. Sci.* **56**, 15844 (2021).
- [87] Y. Ren, L. Hu, Y. Shao, Y. Hu, L. Huang, and X. Shi, Magnetism of elemental two-dimensional metals, *J. Mater. Chem. C* **9**, 4554 (2021).
- [88] L. Liu, S. Chen, Z. Lin, and X. Zhang, A symmetry-breaking phase in two-dimensional FeTe₂ with ferromagnetism above room temperature, *J. Phys. Chem. Lett.* **11**, 7893 (2020).
- [89] D. Pierucci, H. Henck, J. Avila, A. Balan, C. H. Naylor, G. Patriarche, Y. J. Dappe, M. G. Silly, F. Sirotti, A. T. Johnson *et al.*, Band alignment and minigaps in monolayer MoS₂-graphene van der Waals heterostructures, *Nano Lett.* **16**, 4054 (2016).
- [90] W. Zhou, X. Liu, X. Hu, S. Zhang, C. Zhi, B. Cai, S. Guo, X. Song, Z. Li, and H. Zeng, Band offsets in new BN/BX (*X* = P, As, Sb) lateral heterostructures based on bond-orbital theory, *Nanoscale* **10**, 15918 (2018).
- [91] M. H. Chiu, C. Zhang, H. W. Shiu, C. P. Chuu, C. H. Chen, C. Y. Chang, C. H. Chen, M. Y. Chou, C. K. Shih, and L. J. Li, Determination of band alignment in the single-layer MoS₂/WSe₂ heterojunction, *Nat. Commun.* **6**, 7666 (2015).
- [92] V. O. Özçelik, J. G. Azadani, C. Yang, S. J. Koester, and T. Low, Band alignment of two-dimensional semiconductors for designing heterostructures with momentum space matching, *Phys. Rev. B* **94**, 035125 (2016).
- [93] P. K. Srivastava, Y. Hassan, Y. Gebredingle, J. Jung, B. Kang, W. J. Yoo, B. Singh, and C. Lee, Multifunctional van der Waals broken-gap heterojunction, *Small* **15**, e1804885 (2019).
- [94] Q. Zheng, W. A. Saidi, Y. Xie, Z. Lan, O. V. Prezhdo, H. Petek, and J. Zhao, Phonon-assisted ultrafast charge transfer at van der Waals heterostructure interface, *Nano Lett.* **17**, 6435 (2017).
- [95] X. X. Li and J. L. Yang, First-principles design of spintronics materials, *Natl. Sci. Rev.* **3**, 365 (2016).
- [96] G. Gatti, J. Issing, L. Rademaker, F. Margot, T. A. de Jong, S. J. van der Molen, J. Teyssier, T. K. Kim, M. D. Watson, C. Cacho *et al.*, Flat Γ moiré bands in twisted bilayer WSe₂, *Phys. Rev. Lett.* **131**, 046401 (2023).

- [97] V. Vitale, K. Atalar, A. A. Mostofi, and J. Lischner, Flat band properties of twisted transition metal dichalcogenide homo- and heterobilayers of MoS₂, MoSe₂, WS₂ and WSe₂, *2D Mater.* **8**, 045010 (2021).
- [98] M. Angeli and A. H. MacDonald, Gamma valley transition metal dichalcogenide moire bands, *Proc. Natl. Acad. Sci. USA* **118**, e2021826118 (2021).
- [99] D. Pei, Z. Zhou, Z. He, L. An, H. Gao, H. Xiao, C. Chen, S. He, A. Barinov, J. Liu *et al.*, Twist-induced modification in the electronic structure of bilayer WSe₂, *Nano Lett.* **23**, 7008 (2023).
- [100] Y. Sun, S. Luo, X. G. Zhao, K. Biswas, S. L. Li, and L. Zhang, InSe: A two-dimensional material with strong interlayer coupling, *Nanoscale* **10**, 7991 (2018).
- [101] H. Liu, Y. Du, Y. Deng, and P. D. Ye, Semiconducting black phosphorus: Synthesis, transport properties and electronic applications, *Chem. Soc. Rev.* **44**, 2732 (2015).